VIP-producing enteric neurons interact with innate lymphoid cells to regulate feeding-dependent intestinal epithelial barrier functions

Jhimmy Talbot[1], Paul Hahn[1], Lina Kroehling[1], Henry Nguyen[1],
Dayi Li[1], & Dan R. Littman[1,2]

[1]Molecular Pathogenesis Program, The Kimmel Center for Biology and Medicine of the Skirball Institute, New York University School of Medicine, New York, NY 10016, USA
[2]Howard Hughes Medical Institute, New York, NY 10016, USA.

Correspondence: dan.littman@med.nyu.edu

19 **ABSTRACT**

20 **The intestinal mucosa serves as both a conduit for uptake of food-derived**
21 **nutrients and microbiome-derived metabolites and as a barrier that prevents**
22 **tissue invasion by microbes and tempers inflammatory responses to the myriad**
23 **contents of the lumen. How the intestine coordinates physiological and immune**
24 **responses to food consumption to optimize nutrient uptake while maintaining**
25 **barrier functions remains unclear. Here, we describe how a gut neuronal signal**
26 **triggered by food intake is integrated with intestinal antimicrobial and metabolic**
27 **responses controlled by type 3 innate lymphoid cells (ILC3)[1-3]. Food consumption**
28 **rapidly activates a population of enteric neurons that express vasoactive**
29 **intestinal peptide (VIP)[4]. Projections of VIP-producing enteric neurons (VIPen) in**
30 **the lamina propria are in close proximity to clusters of ILC3 that selectively**
31 **express VIP receptor type 2 (VIPR2 or VPAC2). ILC3 production of IL-22, which is**
32 **up-regulated by commensal microbes such as segmented filamentous bacteria**
33 **(SFB)[5-7], is inhibited upon engagement of VIPR2. As a consequence, there is a**
34 **reduction in epithelial cell-derived antimicrobial peptide, but enhanced**
35 **expression of lipid-binding proteins and transporters[8]. During food consumption,**
36 **activation of VIPen thus enhances growth of epithelial-associated SFB and**
37 **increases lipid absorption. Our results reveal a feeding- and circadian-regulated**
38 **dynamic intestinal neuro-immune circuit that promotes a trade-off between innate**
39 **immune protection and efficiency of nutrient absorption. As intestinal pathogenic**
40 **microbes disrupt this neuro-immune inhibitory axis, targeting this pathway may**
41 **enhance intestinal barrier function to prevent invasion by enteropathogens[2,3,9].**

42

43 **MAIN TEXT**

44 Type 3 innate lymphoid cells (ILC3) promote maintenance of intestinal immune and
45 metabolic homeostasis by integrating cytokine-mediated and glia-derived cues and,
46 through the production of IL-22 and other cytokines, conveying information from the
47 luminal microbiota to intestinal epithelial cells (IECs) and cells in the lamina propria [1-
48 3,5,10]. The activation of ILC3 is regulated by cytokines, including IL-23, IL-1β, and TL1A,
49 which are produced by mononuclear phagocytes and induced by intestinal microbe-
50 derived stimuli[5,7,11]. Cytokines produced by activated ILC3, particularly IL-22, support
51 the production of antimicrobial peptides (*e.g*. *RegIIIγ*) and mucin by IECs, ensuring
52 spatial segregation of microbes from the intestinal tissue[12,13]. This microbiota-ILC3-IEC
53 circuit promotes intestinal barrier function by controlling intestinal commensal microbiota
54 and mediating rapid protective responses to enteropathogens[2,3,9,12]. Different subtypes
55 of ILC3s are present within the intestinal lamina propria and are dispersed or in tertiary
56 lymphoid tissue clusters known as cryptopatches (CPs) and isolated lymphoid follicles
57 (ILFs)[14,15] . In perusing transcriptomic datasets of small intestinal ILCs, we noticed in
58 CCR6^{+} ILC3, which comprise the lymphoid tissue inducer (LTi) cells enriched in CPs
59 and ILFs, selective expression of multiple neurotransmitter/neuropeptide receptors and
60 genes related to axonal guidance and neuron differentiation when compared to CCR6^{neg}
61 ILC3 and NCR^{+} ILC3 (Fig. 1a and Extended Data Fig. 1a-c)[16,17]. This prompted us to
62 evaluate whether CCR6^{+} ILC3 in the intestinal lamina propria were associated with
63 neuronal projections from the enteric nervous system (ENS). The ENS is part of the
64 peripheral autonomic nervous system, which controls gastrointestinal functions by

65 promoting rapid gut responses to changes in the luminal compartment (e.g. food intake,
66 microbes, metabolites, etc.[18-22]). We observed that ILC3 in CPs/ILFs were in close
67 proximity to neuronal projections in the lamina propria (Fig. 1b-d and Supplementary
68 Videos 1,2). The CP/ILF-associated neuronal projections were positive for vasoactive
69 intestinal peptide upon staining with specific antibody (VIP, Fig. 1e and Extended Data
70 Fig. 2). We also observed association of VIPen and colonic lymphoid patches
71 (Extended Data Fig. 3a,b). Indeed, ILC3 in CPs/ILFs were closer to VIP^{+} enteric
72 neurons (VIPen) than to neurons positive for substance P or tyrosine hydroxylase
73 (which produce norepinephrine or dopamine) (Fig. 1f and Extended Data Fig. 2). These
74 anatomical findings, together with the fact that CCR6^{+} ILC3 express a high amount of
75 VIP receptor type 2 (*Vipr2*) (Fig. 1a), prompted us to investigate whether signaling from
76 VIPen could modulate CCR6^{+} ILC3 functions and intestinal immune homeostasis.
77 We isolated ILC3 from the lamina propria of the small intestine of C57BL/6 mice
78 (Extended Data Fig. 4a) and observed that *in vitro* activation of VIPR2 inhibited IL-23-
79 induced production of IL-22 by CCR6^{+} ILC3 (Fig. 2a,b and Extended Data Fig. 4b,c),
80 although there was no effect on cell activation (marked by Sca-1 up-regulation) or on IL-
81 22 production by CCR6^{neg} ILC3 (Extended Data Fig. 4d-f). In order to investigate the *in*
82 *vivo* role of VIPR2 activation in CCR6^{+} ILC3 functions, we generated mixed bone
83 marrow chimeric mice reconstituted with a 1:1 ratio of isotype-marked *Vipr2*$^{+/+}$ and
84 *Vipr2*$^{-/-}$ cells. IL-22 was expressed in a greater proportion of *Vipr2*$^{-/-}$ CCR6^{+} ILC3 when
85 compared to *Vipr2*$^{+/+}$ ILC3 (Extended Data Fig 5a,b). We also generated mice with
86 conditional deletion of the gene encoding VIPR2 in ILC3 (*Rorc(t)*^{Cre}*Vipr2*$^{fl/fl}$, or ILC3$^{\Delta Vipr2}$)
87 and found that a larger proportion and number of CCR6^{+} ILC3 isolated from the small

88 intestine of ILC3$^{\Delta Vipr2}$ mice expressed IL-22 than cells isolated from WT littermates (Fig.
89 2c and Extended Data Fig. 5c-f). Epithelial *RegIIIγ* mRNA, regulated by IL-22, was
90 considerably higher in IECs from ILC3$^{\Delta Vipr2}$ mice when compared to WT mice (Fig. 2d),
91 suggesting that VIPen-derived neuropeptide acts through VIPR2 to inhibit ILC3-
92 mediated innate immune responses.

93 To determine whether direct modulation of VIPen (inhibition or activation) could
94 affect ILC3 function, we adopted a chemogenetic strategy utilizing mice engineered to
95 express designer receptors exclusively activated by designer drugs (DREADD)[23]. We
96 selectively expressed inhibitory DREADD (hM4Di) in VIPen of *Vip*$^{IRES\text{-}Cre}$*hM4Di*$^{fl\text{-}stop\text{-}fl/+}$
97 mice and observed a higher frequency of IL-22-producing CCR6^{+}ILC3 at 24h following
98 VIPen inhibition with the DREADD ligand clozapine-N-oxide (CNO, Fig. 2e,f). In parallel,
99 there was increased *RegIIIγ* mRNA expression in the IECs after VIPen inhibition (Fig.
100 2g). Conversely, mice expressing the activating DREADD (hM3Dq) in VIPen (*Vip*$^{IRES\text{-}Cre}$*hM3Dq*$^{fl\text{-}stop\text{-}fl/+}$ mice) had fewer IL-22^{+} cells among the CCR6^{+} ILC3 and lower *RegIIIγ*
102 mRNA in IECs following VIPen activation with CNO (Fig. 2h-j). Combined, these results
103 indicate that VIPen modulates intestinal immune homeostasis, acting through VIPR2 on
104 CCR6^{+} ILC3 to inhibit cell activation and IL-22 production.

105 We next investigated whether alteration of VIPen activity contributes to changes of
106 intestinal barrier function during intestinal colonization with an enteropathogen. As
107 previously described[24], following infection with *Citrobacter rodentium* there was
108 increased *Vip* mRNA expression in the proximal colon and cecum and of VIP amounts
109 in the portal vein, but not in the peripheral blood (Extended Data Fig. 6a-c), suggesting

110 an increase in VIPen activity in the intestinal tissue. Oral gavage of mice with a
111 relatively low dose of *C. rodentium* ($2x10^9$ CFU) is tolerated by mice with an intact
112 immune system. However, DREADD-mediated activation of VIPen during the first 4
113 days of infection led to increased bacterial translocation to the spleen and liver (Fig.
114 2k,l) and resulted in reduced survival (Fig. 2m), despite only a moderate increase in the
115 amount of luminal *C. rodentium* (Extended Data Fig. 6d). Gavage with a high dose of *C.*
116 *rodentium* ($4x10^{10}$ CFU) resulted in large amounts of bacteria that translocated to the
117 liver and spleen (9d.p.i.) (Fig. 2n,o). DREADD-mediated inhibition of VIPen provided
118 substantial protection from bacterial breach of the intestinal barrier without affecting the
119 bacterial burden in the feces (Fig 2n,o and Extended Data Fig. 6e). Moreover, treatment
120 with recombinant murine IL-22 reversed the effect of DREADD-mediated activation of
121 VIPen on mortality and bacterial translocation (Extended Data Fig. 6f,g) Activation of
122 VIPen during the events that follow infection with enteropathogens may therefore be an
123 important contributor to intestinal barrier breakdown, which could be mitigated by
124 inhibition of enteric VIP activity on ILC3.

125 These results suggested the existence of physiological signals that promote
126 activation of VIPen during homeostasis, with consequent tonic inhibition of $CCR6^+$ ILC3.
127 Food ingestion has been reported to rapidly signal VIP release in the intestine[4]. Indeed,
128 we observed a greater amount of VIP in the ileum of mice sampled during the vivarium's
129 dark-phase as compared to the light-phase, which correspond to periods of food
130 consumption and resting, respectively (Extended Data Fig. 7a). Due to the *ad libitum*
131 feeding scheme, approximately 15% of daily food intake occurs during the light-
132 phase/resting period[25]. To dissect the effect of food intake on the VIPen immune

133 inhibitory axis and to reduce the noise created by feeding during the resting period, we
134 restricted food availability for two weeks to alternating 12h cycles of feeding and fasting.
135 To dissociate the effects of light/dark cycles from time of feeding, food was available to
136 a group of mice only during the dark-phase (night-fed mice, ZT12-ZT0/6PM-6AM), while
137 another group had food available only during the light-phase (day-fed mice, ZT0-
138 ZT12/6AM-6PM). Using this scheme, we observed more VIP in the portal vein, but not
139 in the peripheral blood, after 6h of food availability when compared to mice fasted for
140 6h, regardless of whether mice were fed during the light phase (ZT 6) or during the dark
141 phase (ZT 18) (Extended Data Fig. 7b,c). In turn, the frequency of IL-22^{+} CCR6^{+} ILC3
142 was reduced during the periods of food consumption (at 6h of feeding) relative to fasting
143 periods (fasted for 6 h), independently of light-dark cycles (Fig. 3a,b).
144 Using the mixed bone marrow chimeric mice, we observed among the *Vipr2*$^{+/+}$
145 CCR6^{+} ILC3 a reduced frequency of IL-22^{+} cells at 6h after start of food consumption
146 (ZT 18) when compared to mice fasted for 6h (ZT 6) (Fig 3c and 3d). In contrast, there
147 was no difference in frequency of IL-22^{+} cells in the *Vipr2*$^{-/-}$ CCR6^{+} ILC3 population with
148 or without feeding. This is consistent with VIPR2 signaling-dependent inhibition of IL-22
149 production in CCR6^{+} ILC3 following food intake. This conclusion was further supported
150 by the observed reduction in the frequency of IL-22^{+} CCR6^{+} ILC3 at 6h following
151 intragastric delivery of a liquid test diet, but not control saline, during the light-phase
152 period (ZT1-ZT7) (Fig 3e,f). Furthermore, DREADD-mediated inhibition of VIPen
153 abrogated the effect of the test diet on ILC3 (Fig. 3e and 3f). These results suggest a
154 fast and dynamic temporal control of intestinal CCR6^{+} ILC3 function promoted by food
155 intake-mediated activation of VIPen and VIPR2.

156 Because IL-22 acts on intestinal epithelial cells to regulate barrier functions,
157 including their interactions with commensal microbiota, we next examined whether the
158 neuroimmune inhibitory circuit promoted by food consumption influences host-microbial
159 interactions. There was elevated *RegIIIγ* mRNA expression in the IECs in mice fasted
160 for 12h as compared to those fed during that time frame. In parallel, food consumption
161 had a striking effect on the morphology of the ileal epithelium-associated segmented
162 filamentous bacteria (SFB) (Fig. 4a-c and Extended Data Fig. 7d,e). SFB attached to
163 IECs had long segmented filaments after 12h of food consumption, independently of
164 light/dark cycles. However, in the ileum of mice fasted for 12h, independently of light-
165 cycle, epithelium-associated SFB had few segments and were stubble-like. Short-term
166 blockade with α-IL-22 reduced *RegIIIγ* mRNA expression in the IECs of mice during
167 fasting, but not during feeding (Fig. 4c), and prevented control of SFB growth upon food
168 restriction (Fig. 4d). In ILC3$^{\Delta Vipr2}$ mice, which have increased IL-22 production, SFB
169 failed to form segmented filaments even after 12h of food consumption (Fig. 4e,f).
170 These results suggest that VIPen regulate growth of the commensal microbiota by
171 modulating cryptopatch-associated ILC3 in response to food consumption.
172 As IL-22 was recently shown to regulate lipid metabolism[8], at least in part by
173 controlling genes involved in lipid transport, we examined the role of the VIPen-ILC3-IL-
174 22 circuit in lipid absorption. Mice were adapted for 2 weeks to 12h restricted feeding
175 during light or dark cycles and were then gavaged with ^{3}H-triolein following feeding or
176 fasting. Mice that had been fed for 12h absorbed more of the triglyceride than mice
177 fasted for 12h, although there was some effect of circadian regulation (light/dark
178 adaptation) (Extended Data Fig. 7f,g). Expression of mRNAs for proteins associated

179 with fatty-acid/lipid uptake and transport (e.g. *Fabp2*) was lower in IECs from mice that
180 were food-restricted for 12h compared to fed mice (Fig. 4g), in inverse relationship to
181 *RegIIIγ* mRNA (Fig 4c). Moreover, short-term treatment with α-IL-22 during the fasting
182 period reverted the expression of lipid transporters in IEC and ^{3}H-triolein absorption to
183 amounts comparable to those observed with fed mice (Fig 4g,h).

184 The effect of food intake on IEC-dependent lipid absorption was dependent on
185 VIPen inhibition of ILC3, since expression of lipid transporter mRNAs, ^{3}H-triolein
186 absorption, and concentrations of circulating plasma triglycerides were substantially
187 reduced in ILC3$^{\Delta Vipr2}$ when compared to WT mice after 12h of feeding (ZT 0) (Figures
188 4i-k). Finally, continuous intragastric delivery of a liquid test diet for 6h during the light
189 phase period led to an increase in serum triglycerides, which was blocked by DREADD-
190 mediated inhibition of VIPen (Fig. 4l).

191 These results reveal an important neuro-immune circuit in which feeding-activated
192 VIPen antagonize microbiota-dependent CCR6^{+} ILC3 function, resulting in reduced IL-
193 22 production and increased efficiency of lipid absorption. The benefit of greater nutrient
194 acquisition comes at the expense of reduced barrier function, illustrated by susceptibility
195 to enteropathic bacteria and rapid growth of epithelial-associated commensal SFB.
196 Whether the host derives benefit from the reduced anti-microbial activity is unclear,
197 although it may enable bacteria-dependent generation of essential metabolites[26] and
198 vitamins that would be readily absorbed. Since enteric glial cells (EGCs) can secrete
199 factors that act as activators of ILC3 functions[10], it will be important to determine how
200 VIPen and EGCs coordinate antagonistic signals to promote efficient modulation of
201 ILC3-mediated intestinal barrier functions, and also how neural development-associated

202 factors expressed by ILC3 (e.g. *Cntn1*, *Sema3d*, *Bmp2*) contribute to formation of
203 neuro-immune cell units in cryptopatches/ILFs.

204 The mechanism by which the presence of food in the intestinal lumen is sensed and
205 promotes VIPen activation is still unclear, and microbial[27,28], nutritional[4] or mechanical
206 stimuli[29], acting peripherally or by way of the central nervous system, may be
207 responsible for this. The VIP system has been implicated in circadian regulation
208 centrally, as VIPR2 is required for expression of the core clock genes in the
209 suprachiasmatic nuclei of the hypothalamus, and in the periphery, with circadian
210 oscillation of IL-5 and IL-13 production by ILC2 and feeding-associated eosinophil
211 recruitment in lung and gut mucosa[30,31]. While our study highlights the importance of
212 food intake in regulating the VIPen, there is also a light-dependent contribution to the
213 efficiency of lipid absorption, as there was only a partial effect when the feeding cycle
214 was reversed. We therefore cannot rule out an additional role for central or peripheral
215 clock functions independent of VIPen and ILC3.

216 Our results suggest that disturbances in feeding schedules could reduce intestinal
217 barrier functions and promote dysbiosis and at the same time contribute to metabolic
218 inbalance by chronic activation of VIPen. Moreover, enteropathogens may hijack this
219 neuro-immune circuit and reduce intestinal barrier functions, facilitating intestinal
220 colonization. In these scenarios, VIPR2 inhibitors may be valuable therapeutic tools to
221 reduce lipid absorption or enforce the barrier during acute gastrointestinal infections.

222 **Acknowledgements**

223 We thank S.Y. Kim and the NYU Rodent Genetic Engineering Laboratory (RGEL) for
224 generating the mutant mice. We also thank F-X. Liang, J. Sall, C. Petzold and K.

225 Dancel at the Microscopy Laboratory Core for timely preparation of the scanning
226 electron microscopy images, and M. Cammer and Y. Deng for the help with optical
227 microscopy. The Microscopy Core is partially supported by NYU Cancer Center Support
228 Grant NIH/NCI P30CA016087, S10 RR023704-01A1 and NIH S10 ODO019974-01A1.
229 This study benefitted from data assembled by the ImmGen Consortium. This work was
230 supported by the Pew Latin American Fellows program (J.T.), the Helen and Martin
231 Kimmel Center for Biology and Medicine (D.R.L.); and National Institutes of Health grant
232 R01DK103358 (D.R.L.). D.R.L. is an Investigator of the Howard Hughes Medical
233 Institute.
234

235 **Author Contributions**

236 J.T. and D.R.L. designed the study and analyzed the data. J.T. performed the
237 experiments with assistance from P.H. and D.L., H.N. contributed to the feeding
238 experiments, and L.K. performed the bioinformatics analyses. J.T. and D.R.L. wrote the
239 manuscript. D.R.L. supervised the research.
240

241 **FIGURE LEGENDS**

242 **Figure 1. Processes of VIP-producing enteric neurons are in close proximity to *Vipr2*-**
243 **expressing ILC3 within cryptopatches. a,** Heatmap of differentially expressed neural-related
244 genes between intestinal $CCR6^{+}$ ILC3 and $CCR6^{neg}$ ILC3 (Fold change $\geq$ 2, *p-value <0.05,*
245 GSE116092). Color scale is based on normalized read counts. Genes are listed on the right
246 hand margin ranked based on the relative fold change, and color coded: Green:
247 Neurotransmitter/neuropeptide receptors, Blue: genes related to nervous system

248 development/axonal guidance and contact. Expression in other ILC subsets is included for
249 comparison. **b-d,** Representative confocal images from the small intestine of *Rorc(γt)*$^{EGFP/+}$
250 mice show clusters of intestinal ILC3 (cryptopatch) in close proximity to enteric neurons in the
251 small intestine lamina propria (see supplementary video 1 and 2). Pan-neuronal marker: β3-
252 tubulin^{+} (red), ILC3: GFP^{+}TCRβ^{neg} (green and blue, respectively). n=4 mice, 45 ILC3 clusters.
253 **e, f,** Neurochemical code of cryptopatch-associated enteric neurons. (**e**) Representative
254 confocal images from the small intestine of *Rorc(γt)*$^{EGFP/+}$ mice show cryptopatch-associated
255 enteric neurons are positive for VIP. Neurons: β3-tubulin^{+} (red), VIP^{+} (green); ILC3: GFP^{+}
256 (blue).
257
258 **Figure 2. VIPen promote reduction of mucosal barrier function by VIPR2-**
259 **dependent inhibition of CCR6^{+} ILC3. a, b,** Representative FACS plot (**a**) and
260 summaries (**b**) indicating IL-22 expression in purified CCR6^{+} ILC3 after *in vitro* IL-23
261 stimulation with/without VIPR2 agonist ligands. BAY: BAY-559837, VIP: vasoactive
262 intestinal peptide. *P<0.05 and ***P<0.001 (*t-test*). Data are representative of three
263 independent experiments. **c,** Number of IL-22^{+} CCR6^{+} ILC3 present in the ileum of
264 *Rorc*^{Cre} (WT) and *Rorc*^{Cre} *Vipr2*$^{fl/fl}$(ILC3$^{\Delta Vipr2}$).. **P<0.01 (*t-test*), WT: 8; ILC3$^{\Delta Vipr2}$: 6. **d,**
265 Normalized epithelial *Reg3γ* mRNA from ileum of WT and ILC3$^{\Delta Vipr2}$mice. ***P<0.001 (*t-*
266 *test*), WT: 5; ILC3$^{\Delta Vipr2}$: 5. **e-g,** Effect of VIPen inhibition on ILC3 and intestinal epithelial
267 cells (IEC). Representative FACS plot (**e**) and summary (**f**) indicating IL-22 expression
268 in CCR6^{+} ILC3 from the ileum of *Vip*$^{IRES\text{-}Cre}$*hM4Di*$^{fl\text{-}stop\text{-}fl/+}$ mice (DREADD for VIPen

269 inhibition) 24h following treatment with vehicle or CNO (Clozapine-N-oxide, DREADD
270 ligand). Vehicle: n=5, CNO: n=5. **P<0.01 (*t-test*). Data representative of three
271 independent experiments. **g,** Normalized *Reg3γ* mRNA expression in IEC at 24h
272 following treatment. Vehicle: n=3, CNO: n=3. *P<0.05 (*t-test*). Data representative of two
273 independent experiments. **h-j,** Effect of VIPen activation on ILC3 and IEC.
274 Representative FACS plot (**h**) and summaries (**i**) indicating IL-22 expression in $CCR6^{+}$
275 ILC3 from ileum of $Vip^{IRES\text{-}Cre}hM3Dq^{fl\text{-}stop\text{-}fl/+}$ (DREADD for VIPen activation) 24h
276 following the treatment with vehicle or CNO. Vehicle: 6, CNO: 7. **P<0.01 (*t-test*). **j,**
277 Normalized epithelial *Reg3γ* mRNA at 24h following treatment with vehicle or CNO.
278 Vehicle: 7, CNO: 6. *P<0.05 (*t-test*). Data representative of three independent
279 experiments. **k, l,** Dissemination of *C. rodentium* to the (**k**) spleen and (**l**) liver in $Vip^{IRES\text{-}}$
280 $^{Cre}hM3Dq^{fl\text{-}stop\text{-}fl/+}$ mice treated with vehicle or CNO (1mg/Kg, daily) for 4 days post-
281 intragastric infection with $2x10^{9}$ CFU. Log_{10} Colony Forming Units (CFU) of *C.*
282 *rodentium* 9 days post-oral innoculation (9 d.p.i.). Dotted line: limit of detection.
283 ***P=0.0009 and ****P<0.0001, (*Mann-Whitney test*). Vehicle: n=11 (Positive for *C.*
284 *rodentium:* spleen: 6/11, liver: 8/11), CNO: n=9 (Positive for *C. rodentium:* spleen and
285 liver: 9/9). Data representative of two independent experiments. **m,** Survival rates for *C.*
286 *rodentium*-infected $Vip^{IRES\text{-}Cre}hM3Dq^{fl\text{-}stop\text{-}fl/+}$ mice treated with vehicle or CNO (1mg/Kg,
287 daily, 1-4 d.p.i.: blue rectangle). Vehicle: n=11, CNO: n=11. Data representative of three
288 independent experiments. ****P<0.0001 *(Mantel-Cox test*). **n, o,** Bacterial dissemination
289 to the (**n**) spleen and (**o**) liver of $Vip^{IRES\text{-}Cre}hM4Di^{fl\text{-}stop\text{-}fl/+}$ mice treated with vehicle or
290 CNO (1mg/Kg, daily, 1-4 days post-intragastric infection with $4x10^{10}$ CFU of *C.*

291 *rodentium*). Log_{10} CFU at 9 d.p.i. Dotted line: limit of detection. Vehicle: n=8 (Positive for

292 *C. rodentium:* spleen: 8/8, liver: 8/8), CNO: n=7 (Positive for *C. rodentium:* spleen: 1/7,

293 liver: 1/7). ***P=0.0006 (spleen) and ***P=0.0005 (liver) (*Mann-Whitney test*). Data

294 representative of two independent experiments.

295

296 **Figure 3. Feeding reduces IL-22 production by CCR6$^+$ILC3 through activation of VIPen.**

297 **a, b,** Representative FACS plot (**a**) and summaries (**b**) indicating IL-22 expression among

298 CCR6$^+$ ILC3 from the ileum of mice 6h after feeding or fasting, at ZT6 and ZT18. N=5, *P<0.05

299 (*t-test*). Data are representative of two independent experiments. **c,** IL-22 expression by

300 CCR6$^+$ ILC3 from the ileum of CD45.1 *Vipr2*$^{+/+}$:CD45.2 *Vipr2*$^{-/-}$ bone marrow chimeric mice 6h

301 after fasting (fasted, ZT 6) and 6h after feeding (fed, ZT 18). n=7, *P<0.05 (*paired t-test*). Data

302 are representative of two independent experiments. **d,** Ratio of IL-22-expressing cells, relative

303 to Figure 3c, among CCR6$^+$ ILC3 from the ileum of CD45.1 *Vipr2*$^{+/+}$:CD45.2 *Vipr2*$^{-/-}$ bone

304 marrow chimeric mice 6h after fasting (Fasted, ZT 6) and 6 hours after feeding (Fed, ZT 18).

305 n=7, *P<0.05 (*t-test*). **e, f,** Representative FACS plot (**e**) and summaries (**f**) indicating IL-22

306 expression in CCR6$^+$ ILC3 from the ileum of *Vip*$^{IRES\text{-}Cre}$*hM4Di*$^{fl\text{-}stop\text{-}fl/+}$ mice (DREADD for VIPen

307 inhibition). Mice were treated with vehicle or CNO (1mg/Kg) and 30 minutes later were fed by

308 intragastric administration of saline (0.4 mL each 45 min, for 6 h) or Liquid Test Diet (500

309 mg/mL, 0.4mL each 45 minutes, for 6 h). N=4, **P<0.01 (*t-test*).

310

311 **Figure 4. Dynamic regulation of commensal bacterial growth and lipid**

312 **absorption by feeding-dependent VIP production . a, b,** Representative scanning

313 electron microscopy (SEM) images (**a**) of epithelium-associated commensal SFB in the

314 ileum of mice 12h after fasting or feeding at the end of the dark-phase (ZT 0) and the
315 light-phase (ZT 12) and (**b**) measurements of SFB filament lengths. N=3, ****P<0.001 (*t-*
316 *test*). **c,** Normalized epithelial *Reg3γ* mRNA expression in the ileum of mice treated with
317 IgG or α-IL-22 (10mg/Kg) during the feeding period (Fed for 12h: Treated from ZT 12-
318 >ZT 0) or during the fasting period (Fasted for 12h: Treated from ZT 0->ZT 12). Data
319 pooled from 2 independent experiments: Fed IgG1: N=8, Fed α-IL-22: N=8, Fast IgG1:
320 N=8, Fed α-IL-22: N=7, *P<0.05 and **P<0.01 (*t-test*). **d,** SFB length in the ileum of
321 mice treated with IgG or α-IL-22 (10mg/Kg) during the feeding period (Fed for 12h: ZT
322 12->ZT 0) or during the fasting period (Fast for 12h: ZT 0->ZT 12). N= 3, ****P<0.001 (*t-*
323 *test*). **e,f,** Representative **(e)** SEM images of epithelium-associated SFB in the ileum of
324 WT and ILC3$^{\Delta Vipr2}$ mice fed for 12h and **(f)** measurement of bacterial filament lengths.
325 N= 3, ****P<0.001 (*t-test*). **g,** Normalized epithelial mRNA expression of *Fabp2* in the
326 ileum of mice treated with IgG or α-IL-22 (10mg/Kg) during the fasting period (Fasted for
327 12h: Treated from ZT 0->ZT 12). Data pooled from 2 independent experiments: Fed
328 IgG1: N=8, Fed α-IL-22: N=8, Fast IgG1: N=8, Fed α-IL-22: N=7. *P<0.05 and **P<0.01
329 (*t-test*). **h,** Plasma ^{3}H CPM (counts per minute) in 12h fasted mice after gavage with ^{3}H-
330 triolein (1uCi/mice in 200ul of 20% Intralipid). Mice were treated with IgG or α-IL-22
331 (10mg/Kg) during the fasting period (Fasted for 12h: Treated from ZT 0->ZT 12). Data
332 representative of 2 independent experiments. N=4, ***P<0.001 (*two-way ANOVA*). **i, j,**
333 Normalized epithelial mRNA expression of *Fabp2* and *Cd36* (**i**) and plasma triglyceride
334 content (**j**) in 12h fed WT (N=5) and ILC3$^{\Delta Vipr2}$ (N=4) mice**.** *P<0.05 and **P<0.01 (*t-*

335 *test*). **k,** Plasma ^{3}H CPM in 12h fed WT (N=3) and ILC3$^{\Delta Vipr2}$ (N=3) mice after gavage

336 with ^{3}H-triolein. ***P<0.001, (*two-way ANOVA*). **l,** Plasma triglyceride content in *Vip*$^{IRES-}$

337 ^{Cre}*hM4Di*$^{fl\text{-}stop\text{-}fl/+}$ mice (DREADD for VIPen inhibition) after gavage with Saline (0.4

338 mL/each 45 minutes, for 6 hours) or Liquid Test Diet (500 mg/mL, 0.4mL/each 45

339 minutes, for 6 hours). Vehicle: N=5, CNO: N=4. **P<0.01, (*t-test*).

340

341

342 **REFERENCES**

343 1. Constantinides MG. Interactions between the microbiota and innate and innate-like
344 lymphocytes. *J Leukoc Biol.* 2018;103(3):409-419.
345 2. Sonnenberg GF. Regulation of intestinal health and disease by innate lymphoid cells. *Int*
346 *Immunol.* 2014;26(9):501-507.
347 3. Spits H, Cupedo T. Innate lymphoid cells: emerging insights in development, lineage
348 relationships, and function. *Annu Rev Immunol.* 2012;30:647-675.
349 4. Chayvialle JA, Miyata M, Rayford PL, Thompson JC. Effects of test meal, intragastric
350 nutrients, and intraduodenal bile on plasma concentrations of immunoreactive
351 somatostatin and vasoactive intestinal peptide in dogs. *Gastroenterology.* 1980;79(5 Pt
352 1):844-852.
353 5. Sano T, Huang W, Hall JA, et al. An IL-23R/IL-22 Circuit Regulates Epithelial Serum
354 Amyloid A to Promote Local Effector Th17 Responses. *Cell.* 2015;163(2):381-393.
355 6. Savage AK, Liang HE, Locksley RM. The Development of Steady-State Activation Hubs
356 between Adult LTi ILC3s and Primed Macrophages in Small Intestine. *J Immunol.*
357 2017;199(5):1912-1922.
358 7. Longman RS, Diehl GE, Victorio DA, et al. CX(3)CR1(+) mononuclear phagocytes support
359 colitis-associated innate lymphoid cell production of IL-22. *J Exp Med.* 2014;211(8):1571-
360 1583.
361 8. Mao K, Baptista AP, Tamoutounour S, et al. Innate and adaptive lymphocytes
362 sequentially shape the gut microbiota and lipid metabolism. *Nature.*
363 2018;554(7691):255-259.
364 9. Zheng Y, Valdez PA, Danilenko DM, et al. Interleukin-22 mediates early host defense
365 against attaching and effacing bacterial pathogens. *Nat Med.* 2008;14(3):282-289.
366 10. Ibiza S, Garcia-Cassani B, Ribeiro H, et al. Glial-cell-derived neuroregulators control type
367 3 innate lymphoid cells and gut defence. *Nature.* 2016;535(7612):440-443.
368 11. Mortha A, Chudnovskiy A, Hashimoto D, et al. Microbiota-dependent crosstalk between
369 macrophages and ILC3 promotes intestinal homeostasis. *Science.*
370 2014;343(6178):1249288.
371 12. Hooper LV, Littman DR, Macpherson AJ. Interactions between the microbiota and the
372 immune system. *Science.* 2012;336(6086):1268-1273.
373 13. Dudakov JA, Hanash AM, van den Brink MR. Interleukin-22: immunobiology and
374 pathology. *Annu Rev Immunol.* 2015;33:747-785.
375 14. Eberl G, Marmon S, Sunshine MJ, Rennert PD, Choi Y, Littman DR. An essential function
376 for the nuclear receptor RORgamma(t) in the generation of fetal lymphoid tissue inducer
377 cells. *Nat Immunol.* 2004;5(1):64-73.
378 15. Gury-BenAri M, Thaiss CA, Serafini N, et al. The Spectrum and Regulatory Landscape of
379 Intestinal Innate Lymphoid Cells Are Shaped by the Microbiome. *Cell.* 2016;166(5):1231-
380 1246 e1213.
381 16. Pokrovskii M, Hall JA, Ochayon DE, et al. Characterization of Transcriptional Regulatory
382 Networks that Promote and Restrict Identities and Functions of Intestinal Innate
383 Lymphoid Cells. *Immunity.* 2019.

17. Heng TS, Painter MW, Immunological Genome Project C. The Immunological Genome Project: networks of gene expression in immune cells. *Nat Immunol.* 2008;9(10):1091-1094.
18. Furness JB. The enteric nervous system and neurogastroenterology. *Nat Rev Gastroenterol Hepatol.* 2012;9(5):286-294.
19. Muller PA, Koscso B, Rajani GM, et al. Crosstalk between muscularis macrophages and enteric neurons regulates gastrointestinal motility. *Cell.* 2014;158(2):300-313.
20. Cardoso V, Chesne J, Ribeiro H, et al. Neuronal regulation of type 2 innate lymphoid cells via neuromedin U. *Nature.* 2017;549(7671):277-281.
21. Klose CSN, Mahlakoiv T, Moeller JB, et al. The neuropeptide neuromedin U stimulates innate lymphoid cells and type 2 inflammation. *Nature.* 2017;549(7671):282-286.
22. Margolis KG, Gershon MD. Enteric Neuronal Regulation of Intestinal Inflammation. *Trends Neurosci.* 2016;39(9):614-624.
23. Roth BL. DREADDs for Neuroscientists. *Neuron.* 2016;89(4):683-694.
24. Conlin VS, Wu X, Nguyen C, et al. Vasoactive intestinal peptide ameliorates intestinal barrier disruption associated with Citrobacter rodentium-induced colitis. *Am J Physiol Gastrointest Liver Physiol.* 2009;297(4):G735-750.
25. Kohsaka A, Laposky AD, Ramsey KM, et al. High-fat diet disrupts behavioral and molecular circadian rhythms in mice. *Cell Metab.* 2007;6(5):414-421.
26. Smith PM, Howitt MR, Panikov N, et al. The microbial metabolites, short-chain fatty acids, regulate colonic Treg cell homeostasis. *Science.* 2013;341(6145):569-573.
27. McVey Neufeld KA, Perez-Burgos A, Mao YK, Bienenstock J, Kunze WA. The gut microbiome restores intrinsic and extrinsic nerve function in germ-free mice accompanied by changes in calbindin. *Neurogastroenterol Motil.* 2015;27(5):627-636.
28. McVey Neufeld KA, Mao YK, Bienenstock J, Foster JA, Kunze WA. The microbiome is essential for normal gut intrinsic primary afferent neuron excitability in the mouse. *Neurogastroenterol Motil.* 2013;25(2):183-e188.
29. Chayvialle JA, Miyata M, Rayford PL, Thompson JC. Release of vasoactive intestinal peptide by distention of the proximal stomach in dogs. *Gut.* 1980;21(9):745-749.
30. Harmar AJ, Marston HM, Shen S, et al. The VPAC(2) receptor is essential for circadian function in the mouse suprachiasmatic nuclei. *Cell.* 2002;109(4):497-508.
31. Nussbaum JC, Van Dyken SJ, von Moltke J, et al. Type 2 innate lymphoid cells control eosinophil homeostasis. *Nature.* 2013;502(7470):245-248.

428 **METHODS**

429 *Mice*

430 C57Bl/6 mice were obtained from Taconic Farm. All transgenic mice were bred and
431 maintained in the animal facility of the Skirball Institute (New York University School of
432 Medicine) in specific pathogen-free conditions. *hM3Dq*$^{fl\text{-}stop\text{-}fl}$ mice (CAG-LSL-Gq-
433 DREADD, Jax #026220), *hM4Di*$^{fl\text{-}stop\text{-}fl}$mice (CAG-LSL-Gi-DREADD, Jax #026219),
434 *VIP*$^{IRES\text{-}Cre}$ mice (B6J.Vip-IRES-Cre, Jax #031628) and CD45.1 mice (*B6.SJL-Ptprca*
435 *Pepcb/BoyJ*, Jax# 002014) were purchased from Jackson Laboratories. *Rorc*(γt)$^{EGFP/+}$
436 and *Rorc*^{Cre} mice were generated in our laboratory and previously described[14,22]. *Vipr2*$^{-}$
437 $^{/-}$ mice (Jax# 031332) were purchased from Jackson Laboratories and were maintained
438 in a CD45.2 background or were bred with CD45.1 (*B6.SJL-Ptprca Pepcb/BoyJ*) mice,
439 which subsequently generated *Vipr2*$^{-/-}$ CD45.1/2 mice and WT CD45.1 littermates.
440 Conditional VIPR2 knockout (*Vipr2*$^{fl/fl}$) mice were generated using CRISPR-Cas9
441 technology as described below. Mice in all experiments were 6–12 weeks old at the
442 starting point of treatments and all were colonized with SFB. All animal procedures were
443 performed in accordance with protocols approved by the Institutional Animal Care and
444 Usage Committee of New York University School of Medicine or the NIAID as
445 applicable.

446

447 *Generation of ILC3*$^{\Delta Vipr2}$ *mice*

448 Mice carrying *loxP* sites flanking exons 3 and 4 of the Vipr2 gene (*Vipr2*$^{fl/fl}$) were generated
449 using published CRISPR/Cas9 protocols[32,33] at the NYU School of Medicine's Rodent Genetic
450 Engineering Laboratory. Briefly, guide RNAs targeting regions upstream of exon 3 (gRNA_16

451 sequence: GAAATCTCACAACAGATTCG) and downstream of exon 4 (gRNA_23 sequence:
452 TCTCCTCAGAAGCATCGAAT) were designed using the Crispr guide design
453 software (http://crispr.mit.edu/). gRNA recognition sequences were cloned into the pX330
454 vector (a gift from Dr. Feng Zhang, Addgene #42230), using oligos with a T7 promoter
455 containing the gRNA template that were chemically synthetized by IDT (Integrated DNA
456 Technologies). The products of PCR-amplified T7-gRNA were used as templates for in vitro
457 transcription (MEGAshortscript T7 kit, Thermo Fisher Scientific). The gRNAs were purified
458 using the MEGAClear Transcription Clean-up kit (Thermo Fisher Scientific). Two donor
459 templates (ssDNA_1 and ssDNA_2) with 200bp each were chemically synthetized by IDT. The
460 donor templates contained 60bp homology arms flanking a cassete containing a loxP
461 sequence and XhoI or SalI restriction sites, located in the original PAM sequence (mutated
462 PAM). Namely, ssDNA_1 (XhoI) for the region upstream exon 3:
463 (GGATGGCATTTACATAGGACCCCATCCCAGTGGCTGCTCAGAAGAGCACTCACTCCTTA
464 TCCctcgagataacttcgtataatgtatgctatacgaagttatCCGAATCTGTTGTGAGATTTCGAGAACTCATA
465 AGGACTGATAAGGCCACACAACTTGAGC), and ssDNA_2 for the region downstream exon 4
466 (TGATTTCTCCTAGGTCACACTCAGGGAGCATTTCCAGACACTGGAAAACTCCTGAGGCC
467 CgtcgacataacttcgtataatgtatgctatacgaagttatATTCGATGCTTCTGAGGAGACTATAATTAAACCC
468 TGCCTGTGTGAGGCATGGCTTCTGAT). Mice were generated by injection of a mixture of
469 mammalian optimized Cas9 mRNA (100 ng/µl, TriLink Biotechnologies), purified gRNA_16 and
470 gRNA_23 (50 ng/µl, each) and donor templates ssDNA_1 and ssDNA_2 (50ng/ul, each) in
471 injection buffer (10 mM Tris, pH 7.5; 0.1 mM EDTA) into the cytoplasm of C57BL/6J embryos in
472 accordance with standard procedures approved by the IACUC at the NYU School of
473 Medicine. Female CD-1 mice (Charles River) were used as foster mothers. F0 mice were

474 genotyped and sequenced (Sanger sequencing) to identify mice homozygous for both loxP
475 insertions. Founders bearing loxP insertions were then backcrossed at least one time to wild-
476 type C57BL/6J mice generating the *Vipr2*$^{fl/fl}$ mice. For the generation of ILC3$^{\Delta Vipr2}$ mice, *Vipr2*$^{fl/fl}$
477 mice were crossed with *Rorc*^{Cre} mice for the generation of *Rorc*^{Cre} *Vipr2*$^{fl/fl}$ and *Rorc*^{Cre} *Vipr2*$^{+/+}$
478 littermates.
479
480 *VIPen activation/inhibition using DREADDs*
481 To perform chemogenetic activation or inhibition of VIPen, we bred *VIP*$^{IRES\text{-}Cre}$ homozygous
482 mice to *hM3Dq*$^{fl\text{-}stop\text{-}fl}$ mice (DREADD for activation) or *hM4Di*$^{fl\text{-}stop\text{-}fl}$ mice (DREADD for
483 inhibition), generating *VIP*$^{IRES\text{-}Cre}$*hM3Dq*$^{fl\text{-}stop\text{-}fl}$ (VIPen activation) and *VIP*$^{IRES\text{-}Cre}$ *hM3Dq*$^{fl\text{-}stop\text{-}}$
484 ^{fl}*hM4Di*$^{fl\text{-}stop\text{-}fl}$ mice (VIPen inhibition). To perform 24h activation of the DREADDs, mice were
485 treated with Clozapine-N-Oxide (CNO, 1mg/Kg intraperitoneally, TOCRIS) each 12h. Our pilot
486 experiments in C57BL/6 mice (data not shown) revealed that at these dose CNO treatment
487 does not affect ILC3 function. To perform activation of the DREADDs during *Citrobacter*
488 *rodentium* infection, mice were treated daily with CNO (1mg/Kg, intraperitoneally) from day 1 to
489 day 4 after infection.
490
491 *Food restriction protocol*
492 For a period of two weeks, food was made available to mice only for 12h per daily cycle. Mice
493 were kept in two different regimens: Dark-phase fed mice, with food being available between 6
494 PM – 6AM (ZT 12->ZT 0); and light-phase fed, with food being available between 6 AM – 6PM
495 (ZT 0->ZT 12). To avoid littering, at the beginning of the fasting period of each regimen, mice
496 were transferred to a clean cage containing alpha cellulose clean bedding

497 (Shepherd's™ALPHA-dri). Mice were provided with free access to water.

498

499 *Gavage of Liquid Test Diet*

500 Dry powder micro stabilized rodent liquid diet (Test Diet, LD 101) was blended (mechanical
501 blender) vigorously for 30 seconds in saline (NaCl 0.9%) at 0.5g/mL. Mice were gavaged with
502 400ul of this solution using a polyurethane feeding tube (16ga x 38mm, FTPU-16-38-50,
503 INSTECH) every 45 min for 6 h.

504

505 *Generation of bone marrow VIPR2$^{+/+}$/VIPR2$^{-/-}$ chimeric reconstituted mice*

506 Bone marrow mononuclear cells were isolated from CD45.1 *VIPR2*$^{+/+}$ and CD45.2 (or
507 CD45.1/2) *VIPR2*$^{-/-}$ mice by flushing the long bones. Red blood cells were lysed with ACK
508 Lysing Buffer and the remaining cells were resuspended in PBS for injection in at a 1:1 ratio
509 (WT:VIPR2 KO). 4×10^6 cells were injected intravenously into 6 week old CD45.1/2 (CD45.2)
510 mice that were irradiated 4h before reconstitution using 1000 rads/mouse (2x500rads, at an
511 interval of 3h, at X-RAD 320 X-Ray Irradiator). To deplete intestinal ILC3, one day after the
512 bone marrow transfer, mice were treated with InVivoMAb anti-mouse Thy1.2 (200ug/mice for 4
513 consecutive days, Clone 30H12, BioXCell). Experiments were performed 6-7 weeks after the
514 last treatment with α-Thy1.2.

515

516 *Radioactively labeled triglyceride absorption assay*

517 Plasma ^{3}H-CPM (counts per minute) was measured 1-4h after gavage with ^{3}H-Triolein–
518 containing lipid[34]. Briefly, mice were injected with poloxamer 407 (1g/Kg, i.p., Sigma,
519 #16758). After 30 minutes, mice were gavaged with a mixture of 2μCi ^{3}H-Triolein in

520 200ul of 20% intralipid oil emulsion. Blood samples were collected and diluted in Liquid
521 Scintillation Counting cocktail (Ultima Gold) and measured using a Scintillation counter
522 (Beta Counter MicroBeta^2 System, Perkin Elmer).
523
524 *IL-22 in vivo Blockade*
525 For experiments with IL-22 blockade, mice were injected with monoclonal α-IL-22 (Clone 8E11,
526 250μg/mouse, generously provided by Tangsheng Yi, Genentech), 12 hours before sample
527 collection. Control groups received mIgG1 (inVivoMAb, BioXCell).
528
529 *C. rodentium mediated colon inflammation*
530 *C. rodentium* strain DBS100 (ATCC51459; American Type Culture Collection) was grown at
531 37°C in LB broth to OD600 reading between 0.5 and 0.7. *VIP$^{IRES\text{-}Cre}$hM3Dq$^{fl\text{-}stop\text{-}fl}$* (VIPen
532 activation) and C57BL/6 mice were inoculated with 200 µl of a bacterial suspension (2×10^9
533 CFU) by oral gavage. *VIP$^{IRES\text{-}Cre}$ hM3Dq$^{fl\text{-}stop\text{-}fl}$hM4Di$^{fl\text{-}stop\text{-}fl}$* mice (VIPen inhibition) were
534 inoculated with 200 µl of a bacterial suspension (4×10^{10} CFU) by oral gavage. For DREADD
535 experiments, CNO treatment started at 1 day post-infection (d.p.i.) until 4 d.p.i. Mice were
536 followed the next 12 days post-infection (d.p.i.) to measure survival rate. At 9 d.p.i. fecal pellets
537 were collected and the mice dissected to harvest spleen and liver. Samples were weighted and
538 minced on sterile deionized water with Triton 0.1% and filtered on a 70μm cell strainer. The
539 filtered samples were used to measure *C. rodentium* burden with serial dilutions (triplicates) on
540 MacConkey agar plates.
541
542 *Immunofluorescence and Confocal Microscopy*

543 Small intestine from SFB^{+} *Rorc*(γt)$^{EGFP/+}$ mice were Swiss-rolled, fixed for 4h in 4%
544 paraformaldehyde, incubated overnight in 30% sucrose at 4°C, and frozen in embedding
545 medium for frozen specimens (O.C.T, Tissue-Tek, Sakura). Tissue was cut into 30-70 μM
546 sections, blocked in PBST 0.5% (0.5% Triton X-100, 10% normal donkey serum) for 1 h, and
547 incubated overnight using a combination of 3 of the following antibodies for 1 h: α-Vasoactive
548 Intestinal Peptide (1:1000, rabbit polyclonal, 20077, Immunostar), α-Tyrosine Hydroxilase
549 (1:50, rabbit polyclonal, AB152, Millipore), α-Substance P (1:3000, rabbit polyclonal, 20064
550 Immunostar), α-GFP Alexa Fluor 488 (1:500, clone: FM264G, Biolegend), α-TCRβ Brilliant
551 Violet 421 (1:50, Biolegend), α-β-3-Tubulin Alexa Fluor 594 (1:500, clone:AA10, Biolegend).
552 Tissue was washed and when needed incubated with secondary fluorescently labeled
553 antibodies (Donkey Anti-Rabbit Pacific Blue or Alexa Fluor 647) for 2h before nuclear staining
554 with Draq-7 (R&D Systems) or 4′,6-diamidino-2-phenylindole (DAPI, ThermoFisher). Images
555 were acquired using a Zeiss LSM 710 confocal (Carl Zeiss). The imaging data were processed
556 and analyzed using Image J software (NIH, Bethesda, MD). Imaris software version 9.0.1
557 (Bitplane; Oxford Instruments) was used to generated reconstructed 3D images.
558
559 *Isolation of Lamina Propria Lymphocytes (LPLs) from the small intestine*
560 Whole small intestine or the ileum (distal 14cm of the small intestine) was dissected from mice.
561 Mesenteric fat tissue and Peyer's patches were carefully removed from these tissues.
562 Intestinal tissue was opened and extensively cleaned of fecal matter. Following, this tissue was
563 sequentially treated with HBSS 1X (1 mM DTT) at 37°C for 10 min with gentle shaking
564 (200rpm), and twice with 5 mM EDTA at 37°C for 10 min to remove epithelial cells. The EDTA
565 fraction (epithelial cell-enriched) was filtered, centrifuged and suspended in Trizol for further

566 RNA isolation. The remaining tissue was then minced with a scissor and dissociated in RPMI
567 containing 10% FBS, Dispase (0.05 U/ml; Worthington), collagenase (1 mg/ml collagenase II;
568 Roche) and DNase I (100 µg/ml; Sigma) at constant shaking at 37°C for 45 min (175rpm). The
569 digested tissue was then filtered through a 70µm strainer to remove large debris. Viable
570 Lamina Propria Lymphocytes (LPLs) were collected at the interface of a 40%/80%
571 Percoll/RPMI gradient (GE Healthcare).
572
573 *ILC3 in vitro cell culture*
574 $CCR6^{+}$ and $CCR6^{neg}$ ILC3
575 ($DAPI^{neg}CD3^{neg}CD11c^{neg}CD14^{neg}CD19^{neg}TCR\beta^{neg}TCR\gamma^{neg}NK1.1^{neg}KLRG1^{neg}CD127^{+}CD90.2^{+}$)
576 were isolated from small intestine LPLs of C57BL/6 mice using the ARIA II FACS Sorter (BD
577 Biosciences). ILC3 were cultured at 37°C in flat bottom 96 well plates (10^4 cells/well) in RPMI
578 supplemented with 10% heat-inactivated FBS (Hyclone), 50 U penicillin-streptomycin
579 (Hyclone), 2 mM glutamine (Hyclone), 10mM HEPES (Hyclone), 1mM sodium pyruvate
580 (Hyclone) and 50 µM β-mercaptoethanol (Gibco). ILC3 were stimulated with IL-23 (100pg/mL,
581 R&D systems) and/or VIPR2 ligands (BAY-559837: 1-100nM, and VIP: 1nM, TOCRIS) for 16h
582 (37°C), washed, incubated in complete media in the presence of Golgi Plug (BD Bioscience)
583 for 4h (37°C), and stained for membrane extracellular markers in Staining Buffer (PBS FBS2%
584 EDTA 5mM) and for intracellular markers using Cytofix/Cytoperm buffer set following
585 manufacturer's protocol (BD Biosciences). Acquisition of cytometric parameters was
586 performed on an LSRII (BD Biosciences). All data were analyzed using FlowJo Software
587 Version 10 (Tree Star).
588

589 *Antibodies for intracellular staining and flow cytometry*

590 Live/dead fixable blue (ThermoFisher) or DAPI (ThermoFisher) were used to exclude dead
591 cells. The following monoclonal antibodies were purchased from eBiosciences, BD
592 Pharmingen or BioLegend: CD3, CD45.1, CD45.2, TCRβ, CD11c, CD14, CD19, TCRβ, TCRγ,
593 NK1.1, CD127, CD90.2, CCR6, Sca-1 and IL-22. For cytokine analysis, cells were incubated
594 for 4 hours at 37C in RPMI with 10% FBS and GolgiPlug (BD). Cells were stained for surface
595 markers before fixation and permeabilization, and then subjected to intracellular cytokine
596 staining for IL-22 according to the manufacturer's protocol (Cytofix/Cytoperm buffer set from
597 BD Biosciences). Flow cytometric analysis was performed on an LSR II (BD Biosciences) or an
598 Aria II (BD Biosciences) and analyzed using FlowJo software version 10 (Tree Star).

599

600 *Blood collection*

601 Peripheral and portal vein blood were collected under general anesthesia (Ketamine
602 100mg/Kg, Xylazine 15mg/Kg). Peripheral blood was collected through orbital venous plexus
603 bleeding with a glass capillary in a tube containing EDTA (25mM) as an anticoagulant. Plasma
604 was collected after centrifugation of the collected sample and frozen until processing. Surgery
605 was performed to collect blood from the portal vein, which drains the gastrointestinal tract.
606 Briefly, after laparotomy, the portal vein was localized and the blood was collected with a
607 syringe. Portal vein blood was processed following the same protocol above for peripheral
608 blood.

609

610 *Tissue processing for ELISA*

611 Distal Ileum (6 cm from the ileal-cecal junction) or the Large intestine (Cecum + 3 cm of the

612 proximal colon) were collected and extensively washed to clean out fecal matter. The samples
613 were weighed and, using a tissue homogenizer, extracted in PBS Tween 0.1% (with protease
614 inhibitor) and centrifuged to remove tissue debris. The supernatant was frozen until
615 measurement of VIP concentrations in the tissue.
616
617 *ELISA for Vasoactive Intestinal Peptide*
618 VIP content was measured in the blood plasma or homogenized tissue following
619 manufacturer's recommendations (EIAM-VIP-1, RayBiotech).
620
621 *Measurement of plasma concentration of triglycerides*
622 Peripheral blood was collected as described above and plasma was used to quantify
623 triglyceride concentrations following manufacturer's recommendations (Sigma-Aldrich,
624 MAK266).
625
626 *Scanning Electron Microscopy*
627 Scanning Electron Microscopy was performed on 1-1.5 cm pieces from terminal ileum
628 (2cm above the ileal-cecal junction). Intestine was cut open and washed to remove fecal
629 matter, pinned in dental wax and fixed for 2h with a 0.1M sodium cacodylate buffer (CB,
630 pH 7.4) containing 2.5% glutaraldehyde and 2% paraformaldehyde. Samples were post
631 fixed in 1% OsO4 for 2 hours, dehydrated in ethanol, and critical point dried using
632 Tousimis autosamdsri 931 (Rockwille, MD). The dried intestines were put on SEM
633 stabs, sputter coated with gold/palladium by DESK V TSC HP Denton Vacuum
634 (Moorestown, NJ), and images were taken on random locations in the tissue by Zeiss

635 Gemini300 FESEM using secondary electron mode at 5kv. For quantification of SFB
636 length, random fields were selected for measurement using Image J.
637
638 *RNA extraction from intestinal epithelial cells and RT-qPCR*
639 TRNA isolation of ileal epithelial cells was performed using TRIzol following
640 manufacter's instructions (Invitrogen) followed by DNase I (Qiagen) treatment and
641 cleanup with RNeasy MinElute kit (Qiagen) following manufacturer protocols. cDNA was
642 generated using SuperScriptTM IV First-Strand Synthesis System (ThermoFisher).
643 Gene-specific primers spanning exons were used: *Rps17* (F:'5-cgccattatccccagcaag-3'/
644 R:'5-tgtcgggatccacctcaatg-3'), *RegIIIγ* (F:'5-tctgcaagacagacaagatgct-3'/ R:'5-
645 ggggcatctttcttggcaac-3'), *Fabp2* (F:'5-gtctagcagacggaacggag-3'/R:'5-
646 ctccttcatatgtgtaggtctgga-3'), *Cd36* (F:'5-tggccttacttgggattgg-3'/R:'5-
647 ccagtgtatatgtaggctcatcca-3'). Quantitative PCR was performed using the Hot Start-IT
648 SYBRGreen (Affymetrix) on the Roche real-time PCR system (Roche 480). Values were
649 normalized to *Rps17* gene for each sample.
650
651 *Data processing of public available RNA-seq*
652 DESeq2-normalized gene quantification and differential expression analysis were downloaded
653 from GSE116092[16]. Raw counts were downloaded from GSE127267 (ImmGen ULI RNA-seq
654 data)[17] and differential expression analysis was performed using DESeq2. Normalized counts
655 were used for downstream analysis. A cutoff was made based on the normalized counts of a
656 non-expressed gene (*Foxp3*) (GSE116092, cut-off $\leq$ 9 and for GSE127267, cut off <25). A list
657 with neural-associated related genes list was made from 3 databases - KEGG, Amigo2, and

658 G3Cdb. For the KEGG list, all genes involved in the following pathways were included:
659 Glutamatergic synapse, GABAergic synapse, Cholinergic synapse, Dopaminergic synapse,
660 Serotonergic synapse, Long-term potentiation, Long-term depression, Retrograde
661 endocannabinoid signaling, Synaptic vesicle cycle, Neurotrophin signaling pathway, Axon
662 guidance, Circadian rhythm, Circadian entrainment, Neuroactive ligand-receptor interaction,
663 Cell adhesion molecules (CAMs), and cAMP signaling pathway. The Amigo2 list included
664 genes from the following GO classes - vasoactive intestinal polypeptide receptor activity, G
665 protein-coupled peptide receptor activity, nervous system development, positive regulation of
666 neuron projection development, cerebellum development, neuron projection development,
667 anchored component of postsynaptic membrane, and anchored component of presynaptic
668 membrane. The G2Cdb list was formed with genes from the following lists -L00000001,
669 L00000008, L00000060, L00000062, L00000070 and L00000072. GO term analysis of
670 GSE116092[16] was done using g:Profiler. For heat maps, genes were considered differentially
671 expressed with FDR < 0.01 and log2 fold change $\geq$ 2.
672
673 *Statistical analysis*
674 Unpaired two-sided *t-test*, paired two-sided *t-test,* one-way ANOVA with multiple comparisons
675 with Bonferroni correction, two-way ANOVA with multiple comparisons and Bonferroni
676 correction, Mann-Whitney test, Mantel Cox test (for survival curves), were performed to
677 compare the results using GraphPad Software Version 8 (GraphPad Software). No samples
678 were excluded from analysis. We treated less than 0.05 p value as significant. $*P < 0.05$, $** P$
679 < 0.01, $*** P < 0.001$, and $**** P < 0.0001$. Details regarding number of replicates and the
680 definition of center/error bars can be found in figure legends.

681

682

683 **EXTENDED DATA FIGURE LEGENDS**

684

685 **Extended Data Figure 1. Enrichment of transcripts related to nervous system/neural**
686 **functions and development in CCR6^{+} ILC3. a,** Volcano-plot of differentially expressed genes
687 between CCR6^{+} ILC3 and CCR6^{neg} ILC3 isolated from the small intestine of C57BL/6 mice
688 GSE116092[16]. Green: Neurotransmitter/neuropeptide receptors, Blue: genes related to
689 nervous system development/axonal guidance and contact. **b,** Top 10 Gene-Ontology terms
690 from a comparison between subtypes of ILC3 showing enrichment of transcripts related to
691 neuron differentiation and generation in CCR6^{+} ILC3 when compared to CCR6^{neg} ILC3. Green:
692 Neurotransmitter receptors, Blue: genes related to nervous system development/axonal
693 guidance and contact. **c,** Vocano-plot of differentially expressed genes between CCR6^{+} ILC3
694 (enriched in cryptopatches and ILFs[35]) and NKp46^{+} ILC3 (low presence in CPs and ILFs[36])
695 (GSE127267[17]).

696

697 **Extended Data Figure 2. Neurochemical code of the cryptopatch-associated enteric**
698 **neurons in the small intestine lamina propria. a-c,** Representative immunofluorescence
699 images of different subtypes of lamina propria neuronal projections of enteric neurons in the
700 small intestine of *Rorc(γt)*$^{EGFP/+}$ mice. **(a)** Substance P (green) does not represent the neuronal
701 projections (βIII-Tubulin, red) localized inside CPs/ILFs (cluster of GFP^{+} cells, blue) in the
702 lamina propria. **(b)** Tyrosine hydroxylase^{+} neurons (green) are in close proximity but are not
703 the CP-associated neuronal projections (βIII-Tubulin, red) localized inside CPs/ILFs (cluster of

704 GFP$^+$ cells, blue) in the lamina propria. **(c)** Vasoactive Intestinal Peptide$^+$ (green) neurons (βIII-
705 Tubulin, red) are in close proximity and interacting with ILC3 (GFP$^+$, blue) in CPs/ILFs.
706
707 **Extended Data Figure 3. Cryptopatch-associated enteric neurons are also localized in**
708 **the large intestine (colon) lamina propria. a, b** Representative immunofluorescence images
709 of lamina propria neuronal projections of enteric neurons in the large intestine of *Rorc(γt)*$^{EGFP/+}$
710 mice. **(a)** Cluster of ILC3 (GFP$^+$ cells, green) in close proximity of neuronal projections (βIII-
711 Tubulin, red) of the enteric neurons in the colon lamina propria. **(b)** Cluster of ILC3 (GFP$^+$
712 cells, blue) in close proximity of neuronal projections (βIII-Tubulin, red) of the Vasoactive
713 Intestinal Peptide$^+$ enteric neurons (VIPen, green) in the colon lamina propria.
714
715 **Extended Data Figure 4. VIP agonist inhibits *in vitro* IL-22 production by**
716 **CCR6$^+$ILC3. a,** FACS plot showing gating strategy for identification and isolation of
717 CCR6$^+$ or CCR6^{neg} ILC3 (DAPI^{neg}Lin^{neg} CD127$^+$ CD90.2$^+$). **b, c,** *In vitro* activation of
718 VIPR2 alone does not induce cytokine production or activation of CCR6$^+$ ILC3.
719 Representative FACS plots **(b)** and summary **(c)** for surface Sca-1 expression and
720 intracellular IL-22 in small intestine lamina propria CCR6$^+$ ILC3 stimulated *in vitro* for
721 12h with IL-23 (100pg/mL) or different concentrations of the VIPR2 ligand BAY-559837.
722 N= 3, ***P*=< 0.01 (One-way ANOVA). Data are representative of two independent
723 experiments. **d,** *In vitro* activation of VIPR2 does not modulate IL-23-induced Sca-1
724 expression on CCR6$^+$ ILC3. Summary of Sca-1 expression in small intestine lamina
725 propria CCR6$^+$ ILC3 stimulated *in vitro* for 12h with IL-23 (100pg/mL) or different

726 concentrations of the VIPR2 ligands BAY-559837 and VIP (N= 3). **e, f,** *In vitro* VIPR2

727 activation does not affect IL-23-induced IL-22 production by CCR6^{neg} ILC3.

728 Representative FACS plots **(e)** and summaries **(f)** of surface Sca-1 expression and

729 intracellular IL-22 in small intestine lamina propria CCR6^{neg} ILC3 stimulated *in vitro f*or

730 12h with IL-23 (100pg/mL) with/without combination with VIPR2 ligand BAY-559837

731 (1nM) (N= 3). Data are representative of two independent experiments.

732

733 **Extended Data Figure 5. VIPR2 is required for *in vivo* inhibition of IL-22**

734 **production by CCR6^{+}ILC3. a, b,** Mixed bone marrow chimeras, showing **(a)** no

735 difference in frequency and ratio of WT (*Vipr2*$^{+/+}$) vs VIPR2 KO (*Vipr2*$^{-/-}$) CCR6^{+}ILC3 in

736 the ileum of mice receiving equal number of cells (N=17 mice, combined from 2

737 independent experiments) and **(b)** VIPR2-dependent inhibition of IL-22 production in

738 WT (*Vipr2*$^{+/+}$, CD45.1) versus VIPR2 KO (*Vipr2*$^{-/-}$, CD45.2) CCR6^{+} ILC3 in the ileum of

739 chimeric mice. N=11, ****P<0.0001 (*paired t-test*). Data are representative of two

740 independent experiments. **c, d,** Inactivation of *Vipr2* in ILC3 (ILC3$^{\Delta Vipr2}$) does not affect

741 **(c)** frequency or **(d)** number of CCR6^{+} ILC3 in the mouse ileum. WT: N=8; ILC3$^{\Delta ILC3.}$:

742 N=6. **e, f,** Representative FACS plot (C) and summaries (D) indicating frequency of IL-

743 22 expression in CCR6^{+} ILC3 from the ileum of WT and ILC3$^{\Delta Vipr2}$ mice. WT: N=8;

744 ILC3$^{\Delta Vipr2}$: N=6, ***P<0.001 (*t-test*),

745

746 **Extended Data Figure 6. VIPen regulate host resistance to enteropathogenic**
747 ***Citrobacter rodentium*. a,** Normalized *Vip* mRNA expression in the large intestine
748 (cecum and proximal colon) of C57BL/6 mice at different time points after oral infection
749 with *Citrobacter rodentium* ($2x10^9$ CFU). **Day** 0: N=4; Days 2, 4 and 9: N=6. *P<0.05
750 compared to day 0 (one-way ANOVA)**. b, c,** Increased VIP activity in the gastrointestinal
751 tract but not systemically in mice infected with *C. rodentium.* Concentrations of VIP in
752 plasma from the (**b**) hepatic portal vein, which drains the gastrointestinal tract, and (**c**)
753 peripheral blood of mice at different time points after intragastric administration of
754 vehicle or *C. rodentium* ($2x10^9$ CFU). d.p.i: days post-intragastric infection with *C.*
755 *rodentium*. N= 3/group, **P*<0.05 (*t-test*). **d, e** Infectious burden in feces of (**d**) $Vip^{IRES-Cre}hM3Dq^{fl-stop-fl/+}$ (activating DREADD) and (**e**) $Vip^{IRES-Cre}hM4Di^{fl-stop-fl/+}$ (inhibitory
757 DREADD) mice treated with vehicle or CNO (1mg/Kg, daily, 1-4 days post-intragastric
758 infection with $2x10^9$ CFU for activating and $4x10^{10}$ CFU for inhibitory DREADD mice).
759 Log_{10} Colony Forming Units (CFU) of *C. rodentium* 9 days post-oral innoculation (9
760 d.p.i.). Data representative of two independent experiments. Activating DREADD mice:
761 Vehicle: n=11, CNO: n=9. Inhibitory DREADD mice: Vehicle: n=8, CNO: n=7**,** **P*=0.0009
762 (Mann-Whitney test). **f, g,** Exogenous treatment with recombinant murine IL-22 (rmIL-
763 22, 250μg/mouse/day) protects against increase in **(f)** mortality and **(g)** bacterial
764 dissemination induced by VIPen activation of $Vip^{IRES-Cre}hM3Dq^{fl-stop-fl/+}$ mice. ***P=0.0321*
765 *(Mantel Cox test,* survival); ***P*=0.0022 *(*Mann-Whitney test).
766
767 **Extended Data Figure 7. Feeding controls intestinal VIP release, growth of epithelium-**

768 **associated segmented filamentous bacteria, and lipid absorption. a,** Measurement of
769 concentration of VIP in the ileum reveals higher amounts during dark-phase (feeding period,
770 ZT12-ZT0) than in the light-phase (resting period, ZT0-ZT12). N=4, representative of two
771 independent experiments. **b,** Concentrations of VIP in plasma isolated from hepatic portal vein
772 blood of mice fed or fasted for 6 h. Blood samples were collected at two different time-points,
773 during the light-phase period (ZT 6, 12PM) and the dark-phase period (ZT 18, 12AM). N=4,
774 *P<0.05; **P<0.01 (*t-test*). **c,** Concentrations of VIP in plasma isolated from the peripheral
775 blood of mice. Blood samples were collected at two time-points, during the light-phase period
776 (ZT 6, 12PM) and the dark-phase period (ZT 18, 12AM). N=4. **d,** Representative SEM Image
777 (1K and 3K magnification) showing epithelial-attached SFB in the ileum of mice 12 h after
778 feeding (long filaments) or fasting (short-filaments, "stubbles") at ZT 0. **e,** SFB lengths at
779 different time points during the day in mice that had been fed for two weeks during the dark-
780 phase (ZT12-> ZT0) or during the light-phase (ZT0-> ZT12). **f, g,** Plasma ^{3}H CPM (counts per
781 minute) in mice fed or fasted for 12h during the light-phase (ZT 0 – ZT 12, red and green
782 circles) or during the dark-phase (ZT 12 – ZT 0, blue and black circles) and then gavaged with
783 ^{3}H-triolein were sampled at different times (**f**) and the AUC during 4h was determined for
784 individual mice from each group (**g**). AUC: Area under the curve per mL of plasma. N=4 mice
785 per group, *P < 0.05 and ****P < 0.001 (two-way ANOVA).
786

787 **Supplementary Videos**

788 **Supplementary Video 1.** 3D software reconstruction of Figure 1b showing the small intestine
789 of *Rorc(γt)*$^{EGFP/+}$ mice with a cluster of intestinal ILC3 (cryptopatch) in close proximity to enteric
790 neurons. Pan-neuronal marker: β3-tubulin^{+} (red), ILC3: GFP^{+} (green).

791

792 **Supplementary Video 2.** 3D software reconstruction of Figure 1c from the small intestine of

793 *Rorc(γt)*$^{EGFP/+}$ mice showing ILC3 in the cryptopatch in close proximity to enteric neurons in the

794 small intestine lamina propria. Pan-neuronal marker: β3-tubulin^{+} (red), ILC3: GFP^{+} (green).

795

796 **Supplementary References**

797 32. Wang H, Yang H, Shivalila CS, et al. One-step generation of mice carrying mutations in
798 multiple genes by CRISPR/Cas-mediated genome engineering. *Cell.* 2013;153(4):910-
799 918.
800 33. Yang H, Wang H, Jaenisch R. Generating genetically modified mice using CRISPR/Cas-
801 mediated genome engineering. *Nat Protoc.* 2014;9(8):1956-1968.
802 34. Zhang F, Zarkada G, Han J, et al. Lacteal junction zippering protects against diet-induced
803 obesity. *Science.* 2018;361(6402):599-603.
804 35. Lugering A, Ross M, Sieker M, et al. CCR6 identifies lymphoid tissue inducer cells within
805 cryptopatches. *Clin Exp Immunol.* 2010;160(3):440-449.
806 36. Reynders A, Yessaad N, Vu Manh TP, et al. Identity, regulation and in vivo function of gut
807 NKp46+RORgammat+ and NKp46+RORgammat- lymphoid cells. *EMBO J.*
808 2011;30(14):2934-2947.

809

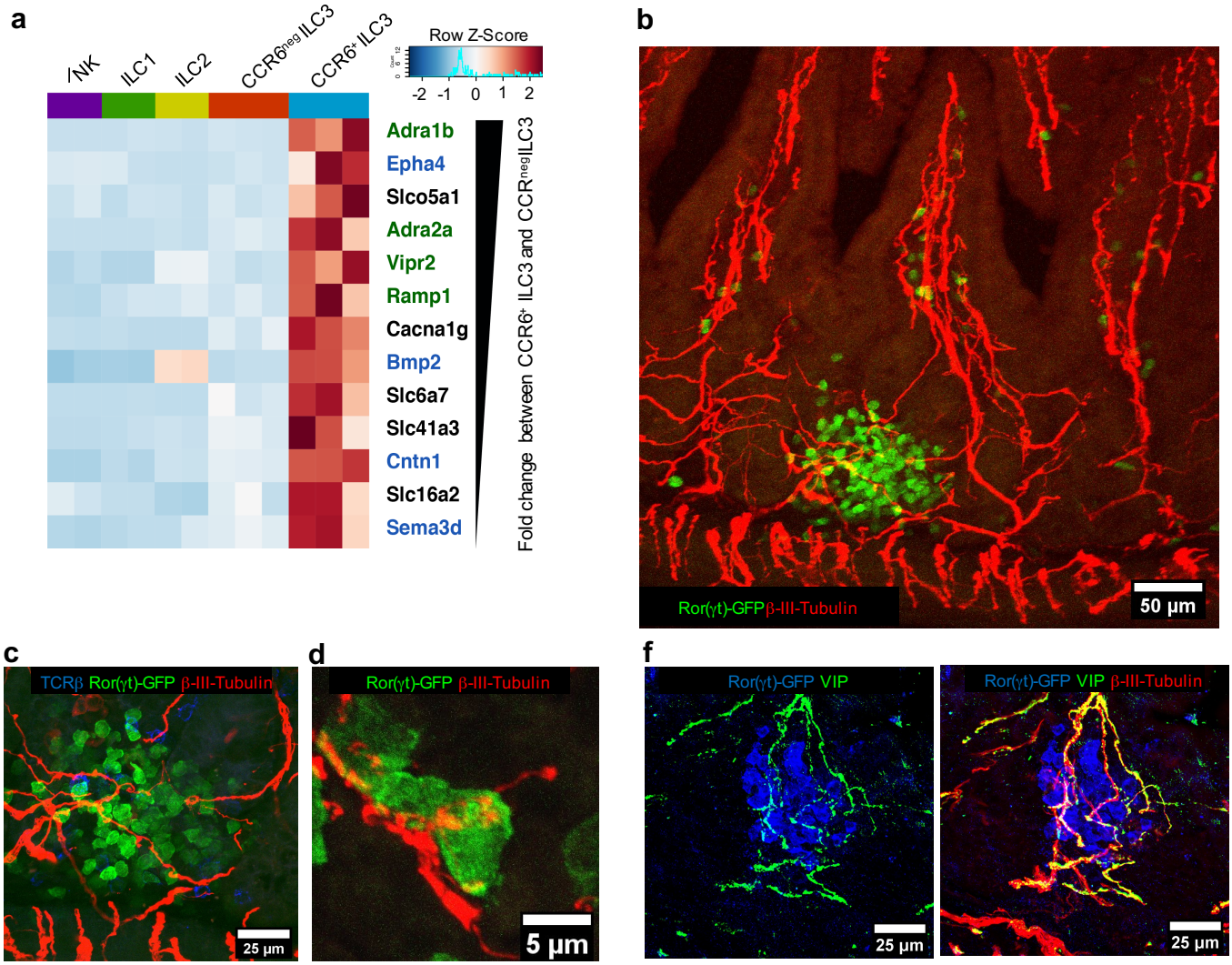

Figure 1. Processes of VIP-producing enteric neurons are in close proximity to *Vipr2*-expressing ILC3 within cryptopatches. a, Heatmap of differentially expressed neural-related genes between intestinal CCR6^{+} ILC3 and CCR6^{neg} ILC3 (Fold change $\geq$ 2, *p-value <0.05,* GSE116092). Color scale is based on normalized read counts. Genes are listed on the right hand margin ranked based on the relative fold change, and color coded: Green: Neurotransmitter/neuropeptide receptors, Blue: genes related to nervous system development/axonal guidance and contact. Expression in other ILC subsets is included for comparison. **b-d,** Representative confocal images from the small intestine of *Rorc(γt)*$^{EGFP/+}$ mice show clusters of intestinal ILC3 (cryptopatch) in close proximity to enteric neurons in the small intestine lamina propria (see supplementary video 1 and 2). Pan-neuronal marker: β3-tubulin^{+} (red), ILC3: GFP^{+}TCRβ^{neg} (green and blue, respectively). n=4 mice, 45 ILC3 clusters. **e, f,** Neurochemical code of cryptopatch-associated enteric neurons. (**e**) Representative confocal images from the small intestine of *Rorc(γt)*$^{EGFP/+}$ mice show cryptopatch-associated enteric neurons are positive for VIP. Neurons: β3-tubulin^{+} (red), VIP^{+} (green); ILC3: GFP^{+} (blue).

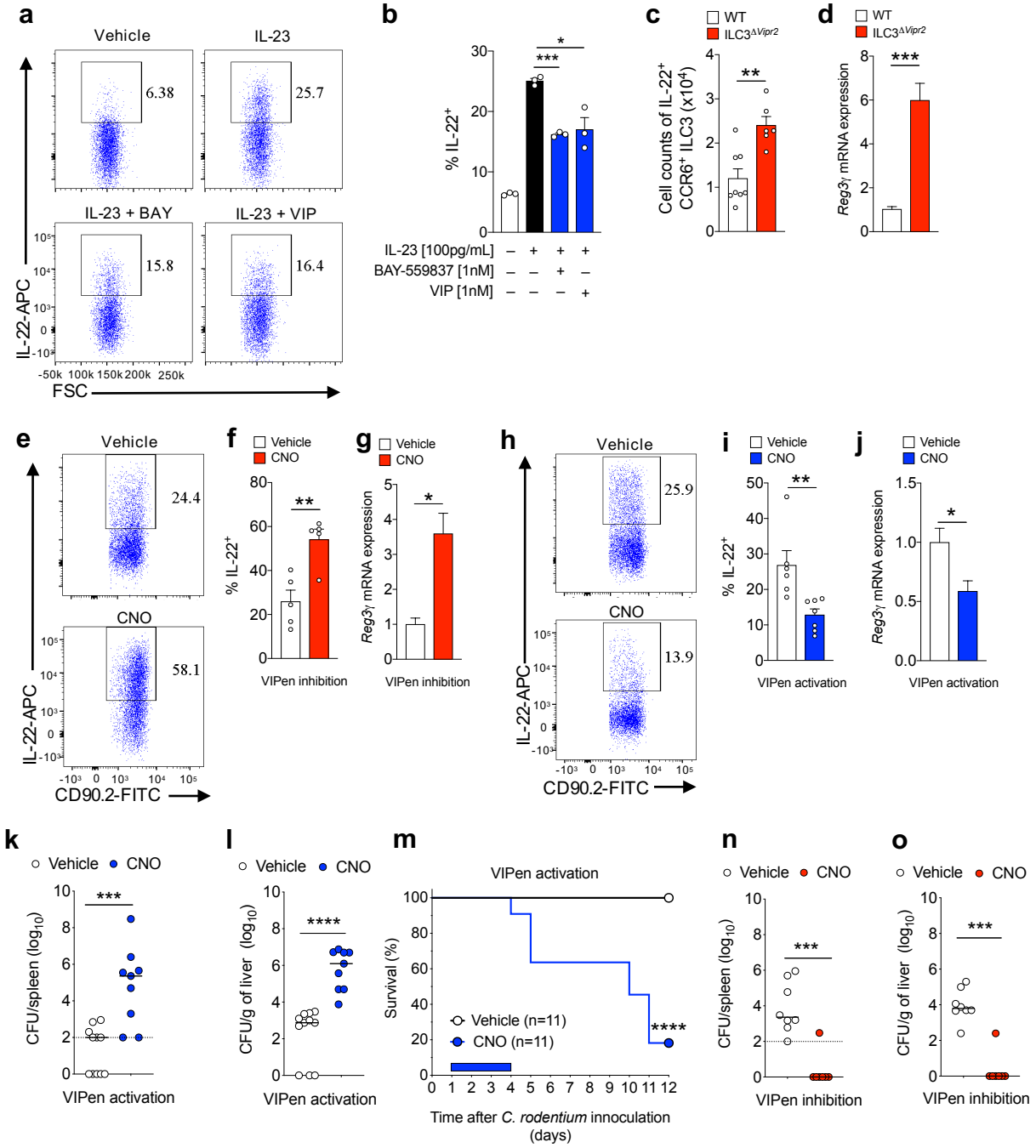

Figure 2. VIPen promote reduction of mucosal barrier function by VIPR2-dependent inhibition of CCR6⁺ ILC3. a, b, Representative FACS plot (**a**) and summaries (**b**) indicating IL-22 expression in purified CCR6⁺ ILC3 after *in vitro* IL-23 stimulation with/without VIPR2 agonist ligands. BAY: BAY-559837, VIP: vasoactive intestinal peptide. **P*<0.05 and ****P*<0.001 (*t-test*). Data are representative of three independent experiments. **c,** Number of IL-22⁺ CCR6⁺ ILC3 present in the ileum of *Rorc*^{Cre} (WT) and *Rorc*^{Cre} *Vipr2*$^{fl/fl}$(ILC3$^{\Delta Vipr2}$).. ***P*<0.01 (*t-test*), WT: 8; ILC3$^{\Delta Vipr2}$: 6. **d,** Normalized epithelial *Reg3γ* mRNA from ileum of WT and ILC3$^{\Delta Vipr2}$mice. ****P*<0.001 (*t-test*), WT: 5; ILC3$^{\Delta Vipr2}$: 5. **e-g,** Effect of VIPen inhibition on ILC3 and intestinal epithelial cells (IEC). Representative FACS plot (**e**) and summary (**f**) indicating IL-22 expression in CCR6⁺ ILC3 from the ileum of *Vip*$^{IRES\text{-}Cre}$*hM4Di*$^{fl\text{-}stop\text{-}fl/+}$ mice (DREADD for VIPen inhibition) 24h following treatment with vehicle or CNO (Clozapine-N-oxide, DREADD ligand). Vehicle: n=5, CNO: n=5. ***P*<0.01 (*t-test*). Data representative of three independent experiments. **g,** Normalized *Reg3γ* mRNA expression in IEC at 24h following treatment. Vehicle: n=3, CNO: n=3. **P*<0.05 (*t-test*). Data representative of two independent experiments. **h-j,** Effect of VIPen activation on ILC3 and IEC. Representative FACS plot (**h**) and summaries (**i**) indicating IL-22 expression in CCR6⁺ ILC3 from ileum of *Vip*$^{IRES\text{-}Cre}$*hM3Dq*$^{fl\text{-}stop\text{-}fl/+}$ (DREADD for VIPen activation) 24h following the treatment with vehicle or CNO.

Continuation Figure 2. Vehicle: 6, CNO: 7. ** *P*<0.01 (*t-test*). **j,** Normalized epithelial *Reg3γ*mRNA at 24h following treatment with vehicle or CNO. Vehicle: 7, CNO: 6. * *P*<0.05 (*t-test*). Data representative of three independent experiments. **k, l,** Dissemination of *C. rodentium* to the (**k**) spleen and (**l**) liver in *Vip*$^{IRES\text{-}Cre}$*hM3Dq*$^{fl\text{-}stop\text{-}fl/+}$ mice treated with vehicle or CNO (1mg/Kg, daily) for 4 days post-intragastric infection with 2x10^{9} CFU. Log_{10} Colony Forming Units (CFU) of *C. rodentium* 9 days post-oral innoculation (9 d.p.i.). Dotted line: limit of detection. *** *P*=0.0009 and ****P<0.0001, (*Mann-Whitney test*). Vehicle: n=11 (Positive for *C. rodentium:* spleen: 6/11, liver: 8/11), CNO: n=9 (Positive for *C. rodentium:* spleen and liver: 9/9). Data representative of two independent experiments. **m,** Survival rates for *C. rodentium*-infected *Vip*$^{IRES\text{-}Cre}$*hM3Dq*$^{fl\text{-}stop\text{-}fl/+}$ mice treated with vehicle or CNO (1mg/Kg, daily, 1-4 d.p.i.: blue rectangle). Vehicle: n=11, CNO: n=11. Data representative of three independent experiments. **** *P*<0.0001 *(Mantel-Cox test*). **n, o,** Bacterial dissemination to the (**n**) spleen and (**o**) liver of *Vip*$^{IRES\text{-}Cre}$*hM4Di*$^{fl\text{-}stop\text{-}fl/+}$ mice treated with vehicle or CNO (1mg/Kg, daily, 1-4 days post-intragastric infection with 4x10^{10} CFU of *C. rodentium*). Log_{10} CFU at 9 d.p.i. Dotted line: limit of detection. Vehicle: n=8 (Positive for *C. rodentium:* spleen: 8/8, liver: 8/8), CNO: n=7 (Positive for *C. rodentium:* spleen: 1/7, liver: 1/7). *** *P*=0.0006 (spleen) and *** *P*=0.0005 (liver) (*Mann-Whitney test*)**.** Data representative of two independent experiments.

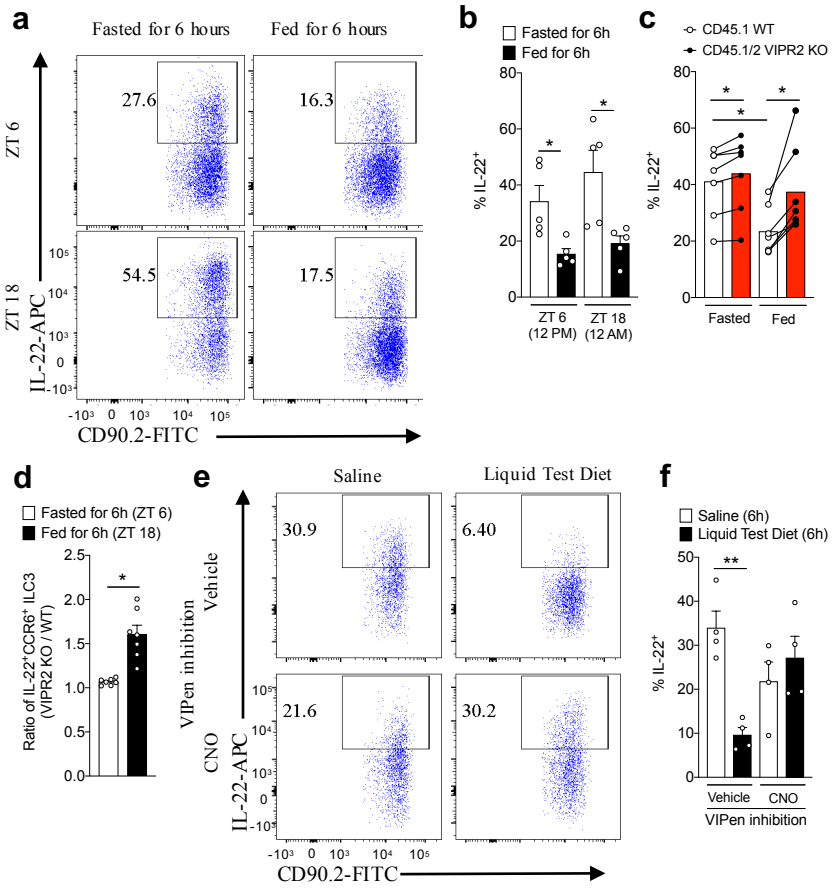

Figure 3. Feeding reduces IL-22 production by CCR6⁺ILC3 through activation of VIPen. a, b, Representative FACS plot (**a**) and summaries (**b**) indicating IL-22 expression among CCR6⁺ ILC3 from the ileum of mice 6h after feeding or fasting, at ZT6 and ZT18. N=5, *P<0.05 (*t-test*). Data are representative of two independent experiments. **c,** IL-22 expression by CCR6⁺ ILC3 from the ileum of CD45.1 *Vipr2*$^{+/+}$:CD45.2 *Vipr2*$^{-/-}$ bone marrow chimeric mice 6h after fasting (fasted, ZT 6) and 6h after feeding (fed, ZT 18). n=7, *P<0.05 (*paired t-test*). Data are representative of two independent experiments. **d,** Ratio of IL-22-expressing cells, relative to Figure 3c, among CCR6⁺ ILC3 from the ileum of CD45.1 *Vipr2*$^{+/+}$:CD45.2 *Vipr2*$^{-/-}$ bone marrow chimeric mice 6h after fasting (Fasted, ZT 6) and 6 hours after feeding (Fed, ZT 18). n=7, *P<0.05 (*t-test*). **e, f,** Representative FACS plot (**e**) and summaries (**f**) indicating IL-22 expression in CCR6⁺ ILC3 from the ileum of *Vip*$^{IRES\text{-}Cre}$*hM4Di*$^{fl\text{-}stop\text{-}fl/+}$ mice (DREADD for VIPen inhibition). Mice were treated with vehicle or CNO (1mg/Kg) and 30 minutes later were fed by intragastric administration of saline (0.4 mL each 45 min, for 6 h) or Liquid Test Diet (500 mg/mL, 0.4mL each 45 minutes, for 6 h). N=4, **P<0.01 (*t-test*).

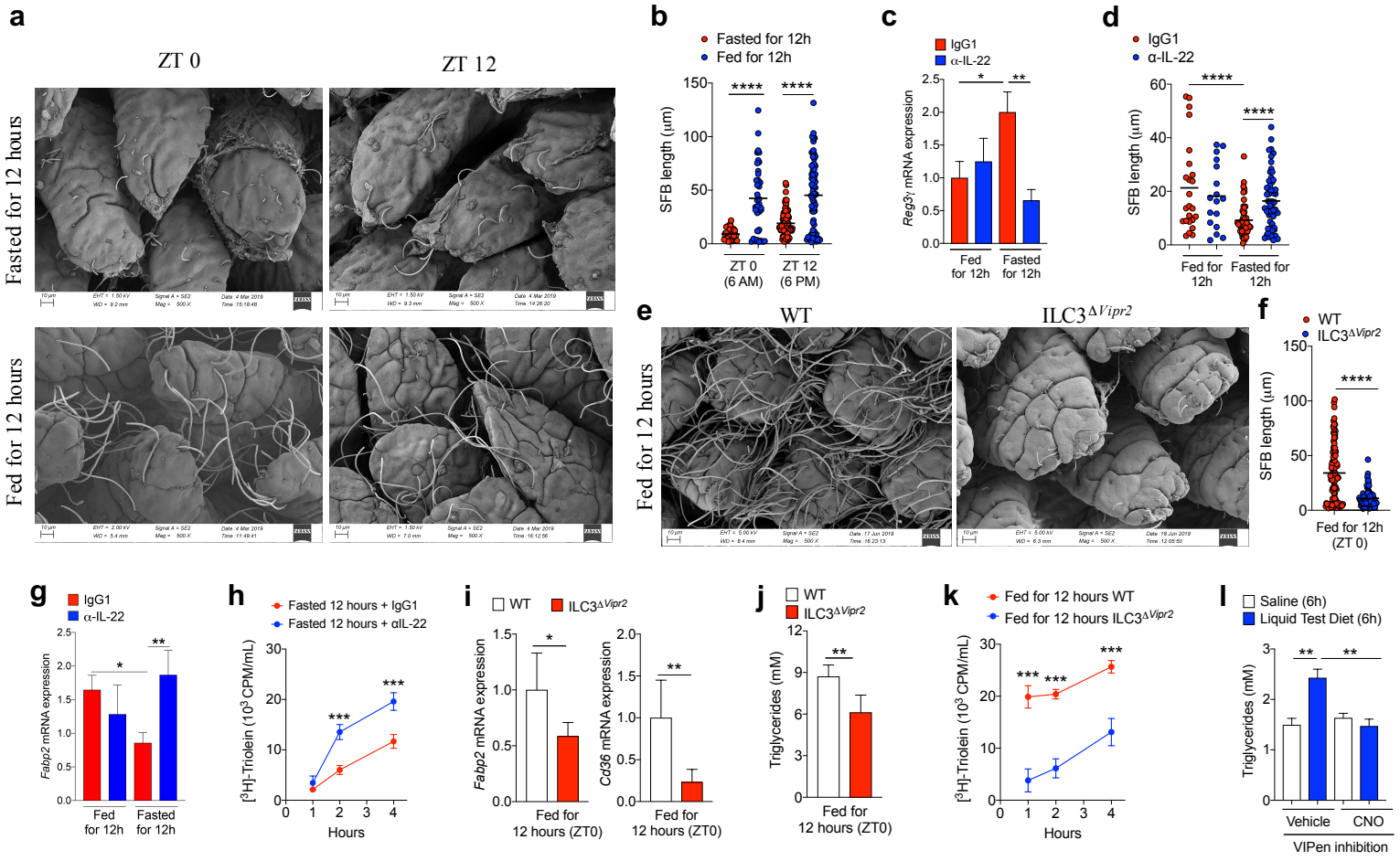

Figure 4. Dynamic regulation of commensal bacterial growth and lipid absorption by feeding-dependent VIP production . a, b, Representative scanning electron microscopy (SEM) images (**a**) of epithelium-associated commensal SFB in the ileum of mice 12h after fasting or feeding at the end of the dark-phase (ZT 0) and the light-phase (ZT 12) and (**b**) measurements of SFB filament lengths. N=3, ****P<0.001 (*t-test*). **c,** Normalized epithelial *Reg3γ* mRNA expression in the ileum of mice treated with IgG or α-IL-22 (10mg/Kg) during the feeding period (Fed for 12h: Treated from ZT 12->ZT 0) or during the fasting period (Fasted for 12h: Treated from ZT 0->ZT 12). Data pooled from 2 independent experiments: Fed IgG1: N=8, Fed α-IL-22: N=8, Fast IgG1: N=8, Fed α-IL-22: N=7, *P<0.05 and **P<0.01 (*t-test*). **d,** SFB length in the ileum of mice treated with IgG or α-IL-22 (10mg/Kg) during the feeding period (Fed for 12h: ZT 12->ZT 0) or during the fasting period (Fast for 12h: ZT 0->ZT 12). N= 3, ****P<0.001 (*t-test*). **e,f,** Representative **(e)** SEM images of epithelium-associated SFB in the ileum of WT and ILC3$^{\Delta Vipr2}$ mice fed for 12h and **(f)** measurement of bacterial filament lengths. N= 3, ****P<0.001 (*t-test*). **g,** Normalized epithelial mRNA expression of *Fabp2* in the ileum of mice treated with IgG or α-IL-22 (10mg/Kg) during the fasting period (Fasted for 12h: Treated from ZT 0->ZT 12). Data pooled from 2 independent experiments: Fed IgG1: N=8, Fed α-IL-22: N=8, Fast IgG1: N=8, Fed α-IL-22: N=7. *P<0.05 and **P<0.01 (*t-test*). **h,** Plasma ^{3}H CPM (counts per minute) in 12h fasted mice after gavage with ^{3}H-triolein (1uCi/mice in 200ul of 20% Intralipid). Mice were treated with IgG or α-IL-22 (10mg/Kg) during the fasting period (Fasted for 12h: Treated from ZT 0->ZT 12). Data representative of 2 independent experiments. N=4, ***P<0.001 (*two-way ANOVA*). **i, j,** Normalized epithelial mRNA expression of *Fabp2* and *Cd36* (**i**) and plasma triglyceride content (**j**) in 12h fed WT (N=5) and ILC3$^{\Delta Vipr2}$ (N=4) mice. *P<0.05 and **P<0.01 (*t-test*). **k,** Plasma ^{3}H CPM in 12h fed WT (N=3) and ILC3$^{\Delta Vipr2}$ (N=3) mice after gavage with ^{3}H-triolein. ***P<0.001, (*two-way ANOVA*). **l,** Plasma triglyceride content in *Vip$^{IRES\text{-}Cre}$hM4Di$^{fl\text{-}stop\text{-}fl/+}$* mice (DREADD for VIPen inhibition) after gavage with Saline (0.4 mL/each 45 minutes, for 6 hours) or Liquid Test Diet (500 mg/mL, 0.4mL/each 45 minutes, for 6 hours). Vehicle: N=5, CNO: N=4. **P<0.01, (*t-test*).